Analysis of positron-annihilation data in Cu and α-$Cu_{1-x}Ge_x$ alloys

L. M. Pecora and A. C. Ehrlich
Naval Research Laboratory, Washington, D.C. 20375
(Received 5 March 1984; revised manuscript received 19 October 1984)

We present momentum densities, $\rho(\bar{p})$, reconstructed from point-geometry positron-annihilation data in Cu and α-$Cu_{1-x}Ge_x$ for $x=0.03$, 0.06, and 0.08. The data deconvolution and subsequent reconstruction processes used are discussed, particularly the errors and limitations inherent in these processes. The results of the analysis of Cu and the α-$Cu_{1-x}Ge_x$ alloy data are then presented as momentum densities in the (110) and (111) planes of these alloys. Non-rigid-band results are found in the "fermiology" as Ge is added to Cu, in particular, the initial shrinking of the Fermi radii along [100] and the bulging of the Fermi surface in the [112] direction. In general, the Fermi surface grows more slowly than a rigid-band rate. The $\rho(\bar{p})$'s also show changes with alloying in the [100] direction in a region beyond the Fermi surface, which suggests other changes in the band structure. We delineate these changes and give evidence that they arise from increases in band hybridization. An analysis of these hybridization effects is given in terms of Cu augmented-plane-wave wave functions obtained from previous self-consistent band-structure calculations.

I. INTRODUCTION

For some thirty years angular-correlation positron-annihilation techniques have been employed to study the conduction- and valence-electron structure of metallic alloys. During most of this period researchers sought to identify the "breaks" in the slope of the coincidence count rate versus γ-ray pair angle. These breaks could then be correlated with and used to determine the position of discontinuities in the occupation of electronic states in $\mathbf{k}$ space, i.e., the Fermi surface. More recently, more elaborate data-processing procedures have been employed to obtain the electron-momentum density, $\rho(\mathbf{p})$, from long-slit and crossed-slit experimental geometries by Mijnarends,[1,2] Berko *et al.*,[3] West *et al.*,[4] and ourselves.[5]

We have carried out the first electron-momentum-density reconstruction in alloys (from crossed-slit-type data) and found that several aspects of the changes of electronic structure with alloy concentration can be sensitively followed in $\rho(\mathbf{p})$. Furthermore, if band- or electronic-structure calculations are available, $\rho(\mathbf{p})$ is a relatively convenient way to make contact with theory. However, to properly interpret the processed data it is essential to understand the effects of the data-handling procedures on the calculated $\rho(\mathbf{p})$. Most of these effects would also apply to positron data other than the crossed-slit type. These effects include possible artifacts of deconvolution procedures and effects of reconstruction on the resolution of $\rho(\mathbf{p})$. These questions have not been previously addressed in the form in which they apply to angular-correlation positron-annihilation research and so are given some attention in this paper. At the same time interpretation of positron-annihilation angular-correlation experiments via the reconstruction of $\rho(\mathbf{p})$ appears very promising.

In this paper we present results of positron-annihilation experiments in Cu and Cu-Ge alloys. We first present the more general results of the reconstruction of the momentum density $\rho(\mathbf{p})$ from the angular correlations of γ rays from the experiments. Secondly, we examine $\rho(\mathbf{p})$ changes in the alloys in detail. Fermi-surface details will be discussed. In addition, we analyze changes in $\rho(\mathbf{p})$ which appear to reflect band-structure changes in regions of $\mathbf{k}$ space removed from the Fermi level. In this case we have shown evidence for changes in s-d hydridization upon alloying Cu with Ge. These latter $\rho(\mathbf{p})$ changes will be related to augmented-plane-wave (APW) wave functions and to the manner in which the s, p, or d component of the wave functions must be varying. Some possible connections to more recent coherent-potential-approximation (CPA) calculations of the band structure will also be discussed.

II. EXPERIMENT

The experimental apparatus is designed to count annihilation radiation using coincidence techniques. The radiation reaching the detectors is restricted by two collimators so as to allow through only γ rays which are in a certain plane with respect to the single-crystal sample. The coincidence detection is done using two 3-in.-diam$\times$4-in.-long NaI(Tl) crystals coupled to photomultiplier tubes and to the usual nuclear instrumentation which counts pulse pairs arriving within a coincidence time window.

The two collimators are different from the usual crossed-slit setups, although they achieve the same purpose. Each collimator is made from four pieces of long rectangular die flat stock (roughly 0.9 m long) which are flat to less than 1 mil per meter. The four pieces are designed to fit together leaving a 2.5×2.5 cm^2 (approximately) square hole along this length. This hole is filled with alternating layers of tantalum tubes and tantalum foil. Enough foil is added to the final layer so that the top piece of flat stock will press down hard enough to prevent the tubes from moving. This results in a matrix of tubes in the 2.5×2.5 cm^2 hole. This matrix does the

collimating of annihilation radiation. Our present apparatus has tubes which are 36 in. long by 70 mil in diameter with a 4-mil wall thickness. This yields a 14×14 matrix of tubes and ostensibly leads to a resolution of 2×2 mrad (FWHM) (full width at half maximum) in momentum space. The collimators are placed on I beams on either side of the sample. The NaI(Tl) detectors sit in lead shielding behind the collimators. A small square hole in the shielding allows each detector to view the γ-ray beam from its collimator. The I beams are connected by a central pivot and are actuated by a stepping motor which thus controls the angle between the collimators. Figure 1 shows the geometric relation of the sample, collimators, and detectors, as well as the coordinates chosen to describe the experiment.

The sample in the experiment is also the source of positrons. The Cu in each sample is activated by placing each sample in the thermal neutron flux of the reactor at the National Bureau of Standards. This creates ^{64}Cu in each sample which has a positron-emitting decay mode (among others) with a 12.8-h half-life. Each sample is cylindrical in shape and is hollow to keep self-absorption to a practical minimum. This sample shape is achieved by lightly cutting with a rotating, circular cross-section tool followed by a heavy acid etching. The cylinder axis is aligned perpendicular to the plane in which the collimators move and so defines the plane of momentum space which is being sampled (see Fig. 1). For example, in the coordinate system of Fig. 1, if the sample cylinder axis is along the [110] crystallographic direction, then the collimated γ rays will carry information about electrons with momentum in the (110) plane of momentum space. Each sample is about 1 cm in length, 1 cm in diameter, and ~6 g in weight, and is activated to ~13 Ci activity. This requires a residence time of about 6 h in the reactor, depending on the exact weight and composition of each sample. The design of the collimators allows one to use samples this large to minimize the residence time in the deleterious environment of the reactor while retaining the resolution and count rate required in this experiment.

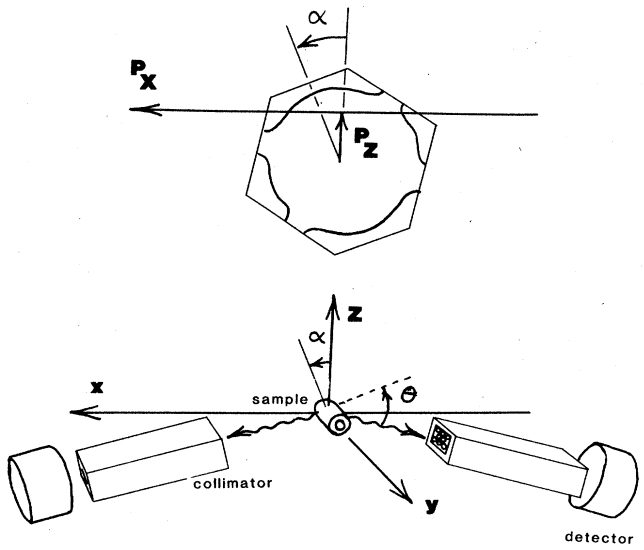

FIG. 1. Apparatus schematic and coordinate system used in experiment. As an example of the sampling of the p space by a measurement at a particular collimator angle θ, the line of integration, p_x, of $\rho(\mathbf{p})$ is shown for Cu in the (110) plane.

The samples are irradiated in the RT-4 pneumatic tube facility at the National Bureau of Standards research nuclear reactor and not annealed thereafter. This facility has a flux of 1.3×10^{13} neutrons/cm^2 sec with a 96% subcadmium energy spectrum. Thus, less than 4% of the neutrons are potentially capable of inducing crystallographic damage. Our ratio $N(0)/N(8)$ (the zero milliradian to eight milliradian count rate), a good measure of irradiation damage, was 4.5 in all samples. This agrees with the results of Senicki and Becker[6] on annealed Cu using an apparatus with similar resolution to our own and an external source of positrons. We have also carried out identical irradiations and measurements twice on the same sample and found no change in our results—further supporting the fact that annealing is not necessary in our work.

This is consistent with the Japanese[7,8] groups that find annealing after irradiation does change their results compared with not annealing. The reactors they use, the position of the samples within the reactors, and the time of irradiation combine to require sample exposure to fast, potentially damaging neutrons which exceeds ours by factors of 25 to 60.

In each experiment six independent directions in the plane defined by the sample cylinder axis are used in sampling the momentum density. Data are taken in each direction for collimator angles from 0 to 13—15 mrad in steps of 0.5 mrad. As a consistency check data are taken in a seventh direction, which is equivalent to one of the first six, usually the first.

The data for each point consist of the total elapsed time T, the time to accumulate the counts for the point ΔT, the number of coincidence counts C_1 for a coincidence window of ~30 ns, τ_1, the number of coincidence counts C_2 for a ~50-ns window, τ_2, and the number of counts accumulated singly from each detector, S_1 and S_2. The two coincidence counts with their respective coincidence windows are used to optimize the statistics. The coincidence window width and the number of single counts from each detector determine the number of accidental coincidence counts and the window width which best minimizes the accidentals while retaining a large number of real coincidence counts is chosen. The real coincidence count rate r, at a particular collimator angle, which is the object of the experiment, is calculated from the relation

$$r_i = C_i/\Delta T - S_1 S_2 \tau_i/(\Delta T)^2$$

for $i=1$ or 2. Here the first term represents the total count rate and the second term the accidental background. This is an approximate solution of the rate equations. For large ΔT (relative to the sample half-life) the rate equations are integrated numerically. We find that the two rates r_1 and r_2 agree well (to within a scale factor) throughout the experiment.

At the beginning of the experiment, when the count rate and thus the number of accidentals is highest, we collect 20 000 coincidence counts per point and use the 30-ns

windows, which generally leads to a statistical error of $\sim 0.7\%$ at 0 mrad and $\sim 1.5\%$ at 12 mrad. As the experiment continues the number of coincidence counts per point taken is lowered in response to the rapidly falling accidental coincidence rate, keeping the statistical error near 1% for points below 8 mrad and no higher than $\sim 1.5\%$ for points above 8 mrad. Towards the end of the run the last direction is taken with 10 000 counts per data point and at this time the accidental count rate is almost negligible.

III. DATA ANALYSIS

The experimental data are first corrected for accidental coincidences and the decay rate of ^{64}Cu. Data for each orientation are then normalized so that the integral over p_z is the same for each. It is then deconvoluted according to the following scheme, applicable but not previously employed in any positron-annihilation experiment. We write here $n_\alpha(p_z)$ for each data point, where α is the orientation angle of the crystal in the plane defined by the crystal cylinder axis (e.g., α is usually taken as the angle between a major symmetry axis in the crystal and the z axis of the experiment—see Fig. 1). The z component of momentum p_z is proportional to θ, the angle the collimators make with each other.

Since we are resolving two components of momentum p_z and p_y (see Fig. 1) with $p_y=0$ but not the third, p_x, and since there is a resolution $R(p_y,p_z)$ associated with the y and z components, the relation between the data $n_\alpha(p_z)$ and $\rho(\mathbf{p})$, the true positron–electron-momentum density becomes

$$n_\alpha(p_z)=\int R(\eta,p_z-\zeta)\rho(\xi,\eta,\zeta)dV\ , \tag{1}$$

where dV is the volume element in momentum space. We find it useful to split Eq. (1) into two integrations in order to deal separately with two data-handling problems which emerge.

The resolution $R(\eta,\zeta)$ in Eq. (1) is factorable into two terms $S(\eta)T(\zeta)$ for our collimators.[9] Since we cannot deconvolute the p_y resolution, $S(\eta)$, we choose $S(\eta)=\delta(\eta)$. Equation (1) becomes (with $p_y=0$)

$$n_\alpha(p_z)=\int_{-\infty}^{\infty} d\zeta\, T(p_z-\zeta)\int_{-\infty}^{\infty} dp_x\rho(\mathbf{p}')\ , \tag{2}$$

where $\mathbf{p}'=(p_x,0,\zeta)$.

In ignoring the effect of the finite resolution in the y direction when we analyze the data, we cannot ignore the potential effect that structure in $\rho(\mathbf{p})$ just out of the $p_y=0$ plane might have on our reconstructed $\rho(\mathbf{p})$ curves. Because we do not take data out of the $p_y=0$ plane, we cannot determine this effect. It is probably small in most regions, but may distort the experimentally determined $\rho(\mathbf{p})$ near the necks in the Fermi surface. However, judging by several figures of $\rho(\mathbf{p})$ displayed below, the distortion near the necks does not qualitatively offset $\rho(\mathbf{p})$. Further, all quantitative measurements are not taken directly from the $\rho(\mathbf{p})$ plots, but are done by scaling all results to those of Cu and then using other, more accurate sources for the Cu values to determine the sizes of similar structures in the alloys. The changes in the sizes of these structures upon alloying are not large compared to overall values of $\rho(\mathbf{p})$. Therefore it is probable that the changes further induced in $\rho(\mathbf{p})$ of the alloys by distortion resulting from p_y finite resolution must be second order compared to the actual changes we measure. This is within our error bars for all quoted quantitative results in this paper.

We solve for $\rho(\mathbf{p})$ by first solving the convolution integral and then reconstructing $\rho(\mathbf{p})$ using our own tomographic techniques.[5] The convolution integral is solved (or deconvoluted) using a statistical regularization method[10,11] which sets an *a priori* condition on smoothness of the solution and enables one to get a good estimate of the error created by the deconvolution. We determine $T(\zeta)$ experimentally. The error estimates showed that our original data error of 1% was magnified to 3% or less at all points. The final effective resolution was calculated to be ~ 1 mrad. However, the total resolution as determined from a detailed comparison of Cu data and a model for $\rho(\mathbf{p})$ of Cu showed the actual effective resolution to be ~ 1.8 mrad. The larger final value comes about because we also have the hidden p_y resolution in $\rho(\mathbf{p})$. Finally, we do not mean to imply that deconvolution can completely make up for lost resolution, but only that it can sharpen the images and make smaller structure prominent. Its use must always include calculation of the corresponding induced error.[11]

Our tomographic reconstruction method[5] yields $\rho(\mathbf{p})$ as a Fourier series in polar coordinates in the sampled plane of momentum space; thus,

$$\rho(\mathbf{p})=\sum_m \rho_m(p)e^{im\phi}\ , \tag{3}$$

where $\mathbf{p}=(p_x,0,p_z)$, $p=|\mathbf{p}|$, and ϕ is the angle of $\mathbf{p}$ in the plane defined by $p_y=0$. The sum over m will have at most as many nonzero terms as there were original data directions, α. There are other methods of reconstruction,[12,13] one of which has been used by Berko *et al.*[3] to reconstruct the momentum density of Cu in several

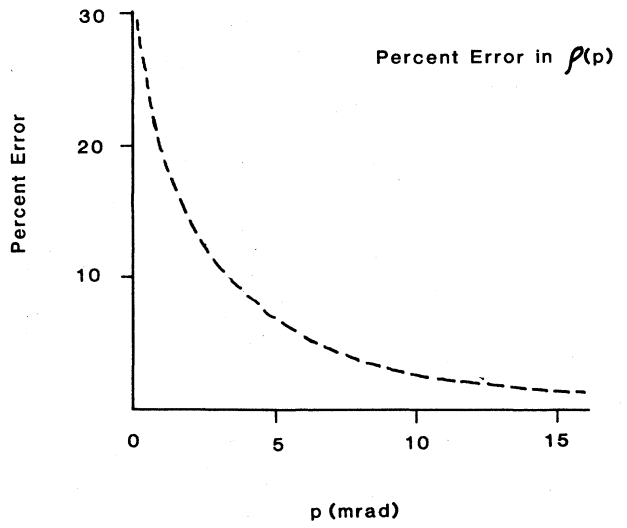

FIG. 2. Total statistical error in the reconstruction of $\rho(\mathbf{p})$ as a function of $|\mathbf{p}|$.

specific directions and in the entire (110) plane.

The error induced by this reconstruction process cannot be calculated directly, as the error induced by the deconvolution process can. However, in Ref. 5 we showed that the statistical errors in the data show up in $\rho(\mathbf{p})$ in a nonlinear fashion, even though they remain localized radially. We used the results of the error analysis of Ref. 5 with the error analysis we did for the deconvolution process to obtain an upper bound on the errors in the reconstructions which is equivalent to all errors adding constructively. The result is Fig. 2, which shows the error in the reconstructed $\rho(\mathbf{p})$ as a function of $|\mathbf{p}|$. Since the statistics for all our data in this paper is very nearly the same, Fig. 2 applies to all reconstructions of experimental data. The error is in terms of percent of absolute magnitude, and so the absolute errors beyond the Fermi surface are seen to be quite small.

A. Cu momentum densities

Experiments and data analyses were first carried out on pure Cu both to test the data-handling procedures and to provide baseline results for interpretation of the alloy data. Figure 3 shows the first six nonzero Fourier coefficients of Eq. (3) for $\rho(\mathbf{p})$ obtained from the (110) data. From symmetry only even cosine terms contribute, so that angular resolution in $\rho(\mathbf{p})$ would be of order $\pi/10$. Note that the higher-frequency terms obtained here are contributing little to the shape of $\rho(\mathbf{p})$.

Figure 4 shows $\rho(\mathbf{p})$ as reconstructed along three major symmetry directions using the ρ_m from Fig. 2. The large peaks at 5 mrad are the result of many-body effects which enhance the annihilation rate near the Fermi surface. The rapid falloffs near 5—6 mrad represent the Fermi-surface radii, and their relative positions are exactly as expected from traditional fermiology studies. Additional anisotropies are also observed beyond the Fermi breaks, i.e., they arise from the lower-energy, fully occupied "d bands." One is between the [110] and [001] directions in the (7—8)-mrad region and this has been discussed earlier by Mijnarends,[1,14] Berko *et al.*,[3] and ourselves.[15] Another is at ~ 8 mrad between the same directions and arises from the onset of the next higher momentum component in the [001] direction. These features and others not seen in the usual two-dimensional plots in high-symmetry directions are shown in a more general setting in Fig. 5, where we display $\rho(\mathbf{p})$ as obtained for pure Cu in the entire (110) plane.

Finally, various checks were made to verify that none of the features in $\rho_m(\mathbf{p})$ result from our experimental or data-handling procedures. For example, nondeconvoluted data were reconstructed and, also, $\rho(\mathbf{p})$ was reconstructed using data in fewer directions. In all such checks results were either unchanged within experimental error or they changed in precisely the expected way.

A sample of pure Cu was also produced with the sample cylinder axis along $[\bar{1}11]$. The momentum density in (111) is reconstructed in Fig. 6 from data taken in six directions using this sample. The $(\bar{1}11)$ plane has a sixfold symmetry (this is in the central plane only). This

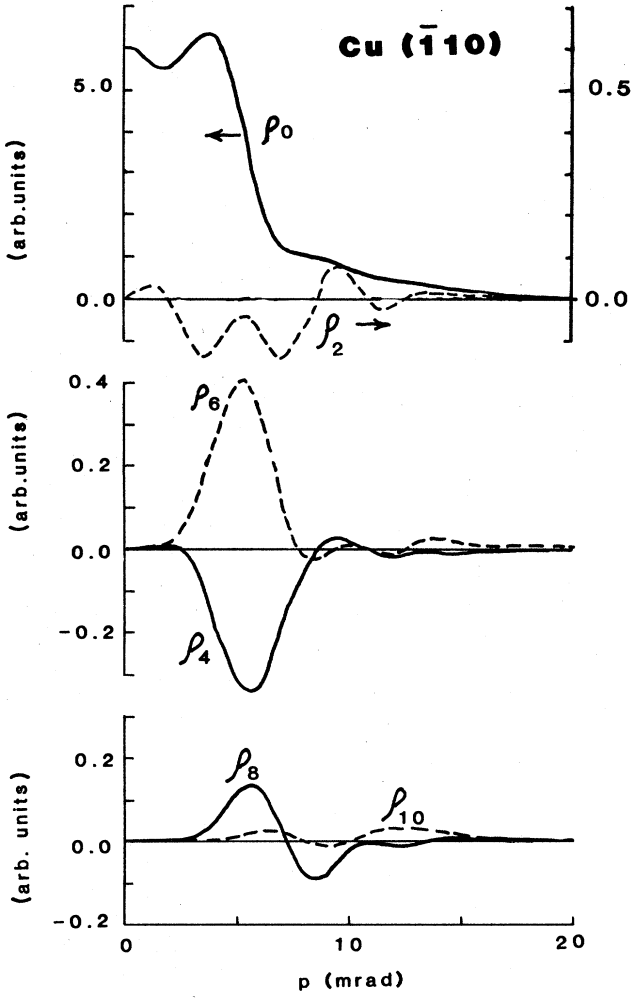

FIG. 3. Fourier components of $\rho(\mathbf{p})$ in $(1\bar{1}0)$ for Cu. Note that the scale changes by a factor of 10 for ρ_2 through ρ_{10}, so that $\rho_{10}(\mathbf{p})$ is quite small, for example.

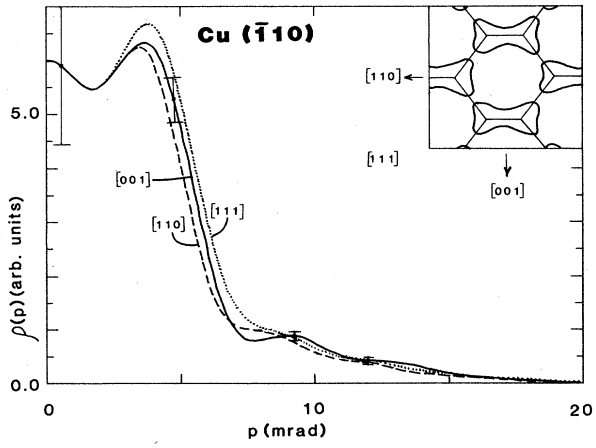

FIG. 4. Sections of $\rho(\mathbf{p})$ along three high-symmetry directions in $(1\bar{1}0)$. Error bars are calculated from Fig. 2 and scaled to $\rho(\mathbf{p})$.

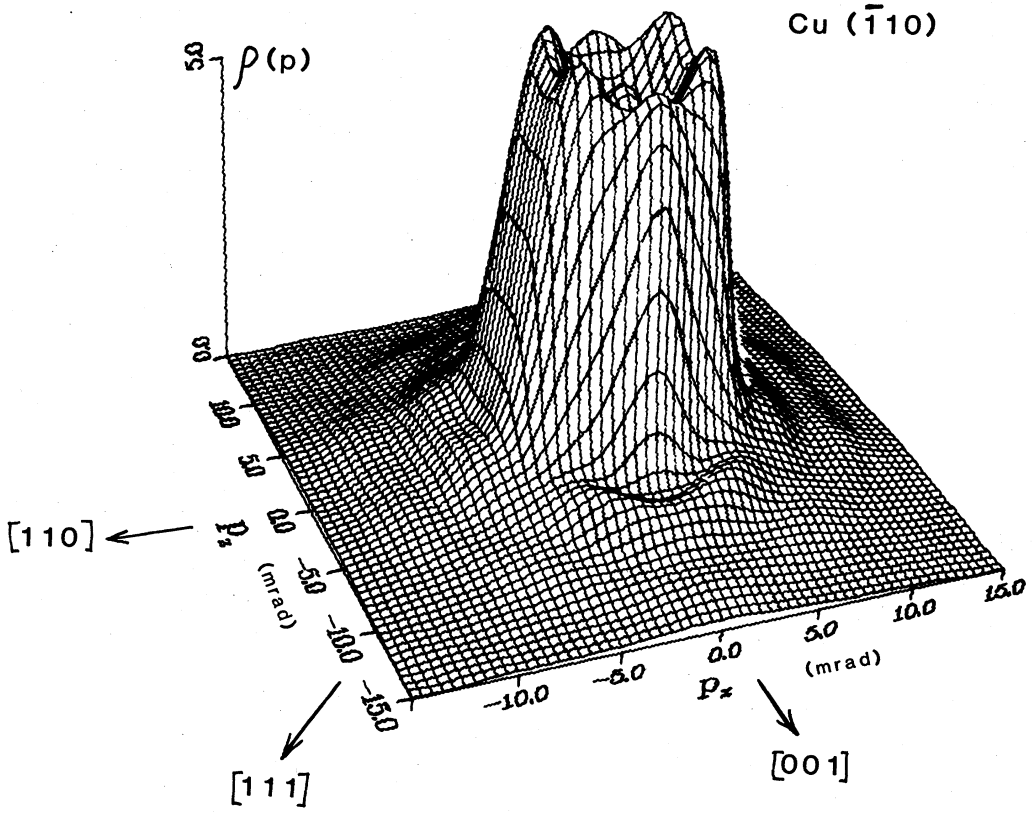

FIG. 5. Reconstruction surface plot of $\rho(\mathbf{p})$ in $(1\bar{1}0)$. Note the details like the necks (three of which are visible), the [002] HMC, and the trough between the first-zone Fermi break and the [002] component.

means that the Fourier series for $\rho(\mathbf{p})$ is a cosine series with only every sixth term contributing $(\rho_0,\rho_6,\ldots,\rho_{30})$ or that the reconstruction has an angular resolution of $\pi/30$, or 6°. In this plane the [110] direction again has the smallest Fermi radius p_F and increases monotonically to the [211]. There are also some anisotropies at momenta beyond p_F. In the [211] direction there is a higher-momentum component (HMC) of the conduction band

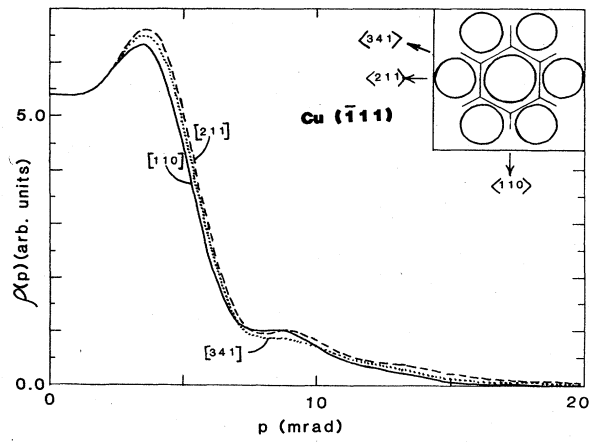

FIG. 6. Sections of $\rho(\mathbf{p})$ for Cu$(\bar{1}11)$ reconstruction.

which is a slice off the top or bottom of the next-zone Fermi surface located at [111], which is not in the $(\bar{1}11)$ central plane (see inset of Fig. 6). This leads to a local minimum at ~8 mrad and a local maximum at ~9 mrad for $\rho(\mathbf{p})$ along [211]. This can be compared to the [110] direction, which is fairly flat in this region. The anisotropy resembles that of the [110]/[001] anisotropy in the $(\bar{1}10)$ results, but is not so dramatic. The [211] and [110] directions are also in the $(\bar{1}10)$ reconstruction, and thus permit a comparison and a further check on the accuracy of the experiment. Both directions in the $(\bar{1}11)$ reconstruction compare favorably with their counterparts in the $(\bar{1}10)$ reconstruction in that their graphs fall nearly on top of each other when presented together.

B. Cu-Ge alloys momentum densities

Samples with three different concentrations of Cu and Ge were used in experiments to determine $\rho(\mathbf{p})$ in $(\bar{1}10)$ for 3, 6, and 8 at.% Ge. One $(\bar{1}11)$ sample of $Cu_{92}Ge_8$ was also used to generate data to reconstruct $\rho(\mathbf{p})$ in $(\bar{1}11)$. Details of changes in these systems are covered in the following sections. Here we only note major changes in $\rho(\mathbf{p})$ between pure Cu and $Cu_{92}Ge_8$.

Figure 7 shows the reconstruction of $\rho(\mathbf{p})$ for $Cu_{92}Ge_8$ in the $(\bar{1}10)$ plane. The order of the curves near the drop-off at 5—6 mrad remains the same as pure Cu. The

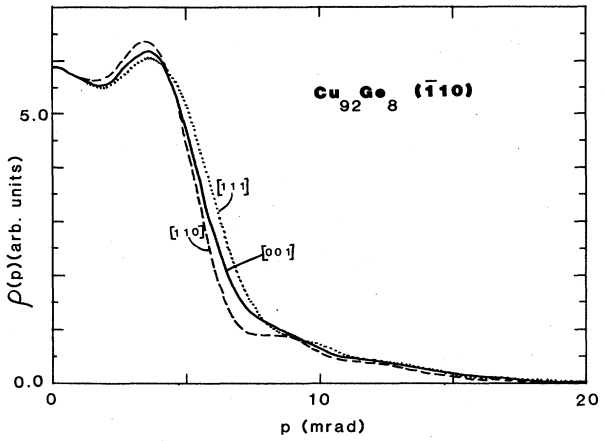

FIG. 7. Sections of $\rho(\bar{p})$ in $(1\bar{1}0)$ for $Cu_{92}Ge_8$.

[110]/[001] anisotropy between ~7—8 mrad, however, has completely reversed. This is a large effect compared to other changes that take place as a result of alloying (e.g., Fermi-surface movement). The [110] direction is almost unchanged from the pure Cu result. It is the [001] direction which has undergone a large change. This can be seen in Fig. 8, where the trough near p_F[100] for Cu is replaced with a bulge in this region. It is evident from Fig. 8 that for the most part $\rho(\mathbf{p})$ does not change radically elsewhere.

The results from the [111] sample are shown in Fig. 9. Again, the order of the Fermi breaks remains the same as Cu. Here, too, the anisotropies beyond p_F have changed when compared to Cu, with the [211] losing its minimum and with the minimum rising just above the comparable [110] values around 8 mrad. This is not at all as large a change as the similar change in [001] for $\rho(\mathbf{p})$ in $(\bar{1}10)$ and is almost surely due here to a resolution effect which smears $\rho(\mathbf{p})$ and thus makes the gap between the first-zone Fermi break and the HMC along [211] appear to fill in as p_F[211] increases with alloying.

C. Fermiology

Features of the Fermi surfaces of the Cu and Cu-Ge alloys have been obtained by examination of $\rho(\mathbf{p})$. The Fermi radii in various directions have been taken as the "average" position of the Fermi break; i.e., the average of $\mathbf{p}$ for which $\rho(\mathbf{p})$ is between 2 and 5 of the arbitrary units of Fig. 4. These limits on $\rho(\mathbf{p})$ were chosen to provide the largest interval for averaging consistent with remaining entirely within the Fermi-break region.

All results to be presented depend on the normalization procedure, but, in fact, the dependence is very weak. Were the Fermi breaks in $\rho(\mathbf{p})$ really vertical, there would be no dependence at all on normalization, and apparently

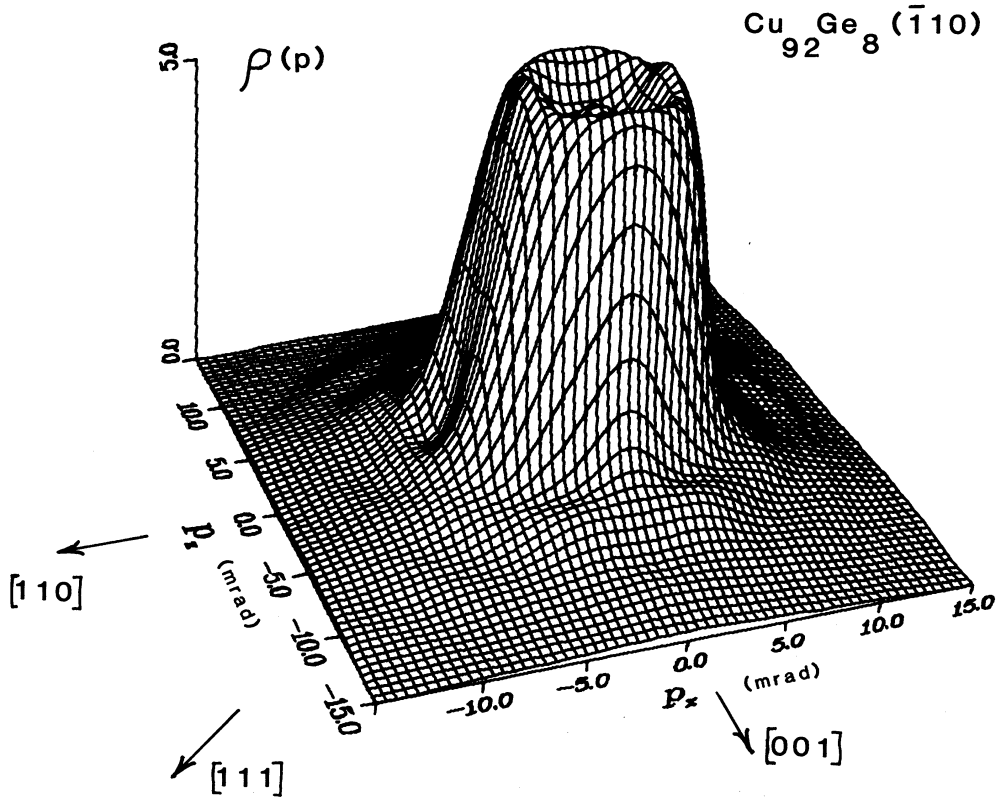

FIG. 8. Surface plot of $\rho(\mathbf{p})$ in $(1\bar{1}0)$ plane for $Cu_{92}Ge_8$.

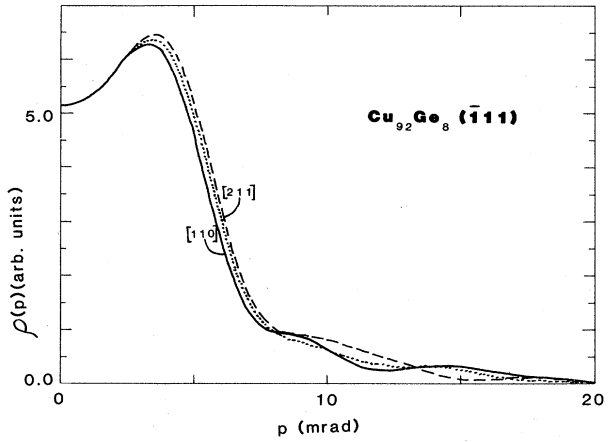

FIG. 9. Sections of $\rho(\mathbf{p})$ in $(\bar{1}11)$ for $Cu_{92}Ge_8$.

they are steep enough to make the dependence almost negligibly weak. For example, a huge 25% error in scale would lead to a shifting in the radius by only 0.1 mrad. Finally, the absolute values of p_F in the alloys are obtained by scaling to our Cu results and the known values in pure Cu.[16]

To determine the Fermi-surface neck dimensions we view the neck edges as a step function of momentum density in the polar-angle direction. Since our six-term expansion of $\rho(\mathbf{p})$ provides 18° resolution, it will smear out the necks to a broader hump-shaped object. We established how a truncated (six-term) Fourier series of a neck relates to the width of the real neck empirically by using a Fermi-surface model consisting of a circle of radius equal to the Γ to L distance with appropriately placed necks of varying widths.

Figure 10 shows the Fermi radii for $Cu_{1-x}Ge_x$ ($x=0.03$, 0.06, and 0.08) in four high-symmetry directions in $(\bar{1}10)$ as determined by the technique described above. Included also are data from McLarnon and Williams[17] for $p_F[110]$ and Suzuki *et al.*[18] for $p_F[001]$. We have also included rigid-band results based on a self-consistent APW calculation for Cu.[19,20] Lattice expansion is taken into account for the rigid-band results. The error bars here are $>\pm 0.1$ mrad, based on our error analysis, and tend to be somewhat pessimistic.

As can be seen from these results, it appears as though the Fermi surface of $Cu_{1-x}Ge_x$ grows more slowly than the rigid-band model in all directions shown. While this does not agree with the results of McLarnon and Williams[17] for $p_F[110]$, it agrees very well with the results of Suzuki[18] including the *decrease* in $p_F[001]$ for the 3-at.% Ge alloy. We note that Prasad and Bansil[21] have done a CPA calculation on the α-Cu-Ge alloy system and have predicted that the Fermi radius along [001] would grow by about one-half its rigid-band rate at low Ge concentrations. The reason for this is the appearance of an impurity band below the Cu conduction band whose states act localized at low concentrations and delocalize at higher concentrations.[21] The overall effect of the impurity band is also to lessen the growth rate of p_F in other directions

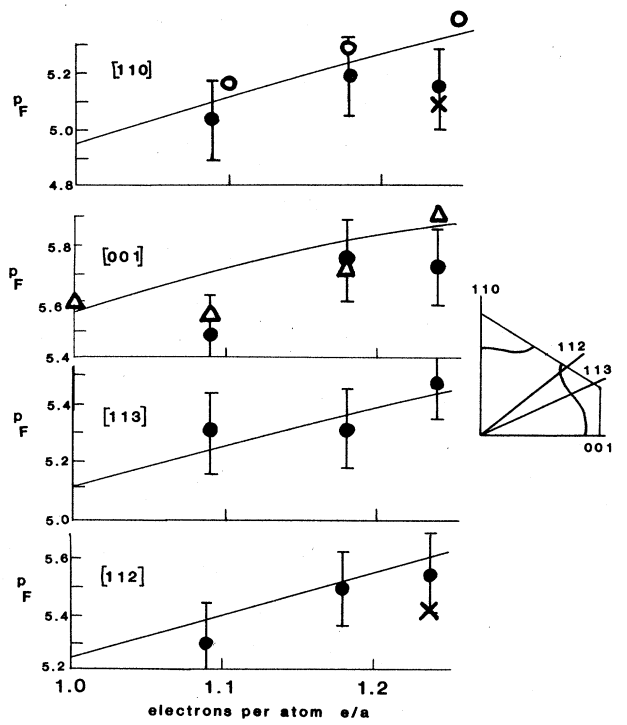

FIG. 10. Fermi radii for high-symmetry directions in $(\bar{1}10)$ (solid circles) and $(\bar{1}11)$ (crosses). Open circles are results of McLarnon and Williams (Ref. 7) and triangles are results of Suzuki *et al.* (Ref. 8). Solid line denotes rigid-band results (Refs. 9 and 10).

by providing states for additional electrons below the Fermi level. The only caution we would have about the radii in Fig. 10 is that the values of p_F for [112] probably contain the greatest error, since the Fermi surface along this direction is not normal to the radial direction, but is turning tangent to it in forming the nearby neck (see inset of Fig. 10).

Figure 11 shows the neck radius as a function of Ge concentration. The rigid-band results are from Bansil *et al.*[22] We include the results of McLarnon and Will-

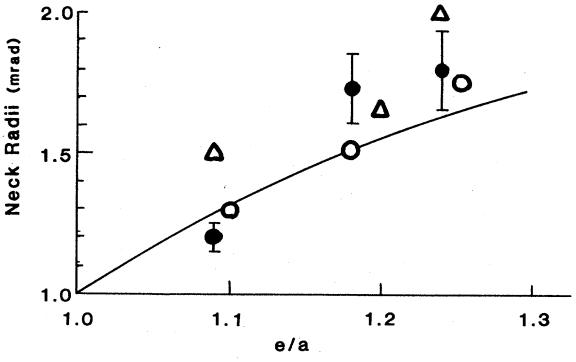

FIG. 11. Neck radii from (110) data vs electrons per atoms. Solid line denotes rigid-band results (Refs. 9 and 10).

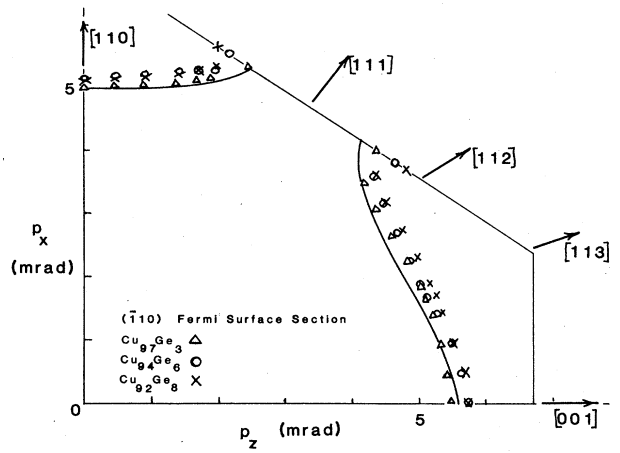

FIG. 12. ($\bar{1}$10) slice of Fermi surface for ^{4}Cu and $Cu_{1-x}Ge_x$, with $x=0.03$ (△), 0.06 (○), and 0.08 (×).

iams[17] and the data of Suzuki *et al.*[18] for comparison. Agreement of all these experimental studies is fairly good and the Fermi surface in this region appears to grow somewhat faster than the rigid-band results.

Figure 12 shows a ($\bar{1}$10) section of the Fermi surface determined by calculating p_F every 5°, as well as along the high-symmetry directions and by using Fig. 11 for the neck values. The rapid growth of the necks compared to other radii is evident. It further appears that a slight bulge develops in the [113] direction.

We have also obtained the Fermi surface for an 8-at. % Ge sample in (111). Only one concentration of Ge, 8 at. %, has been used here. Figure 10 contains points from the [110] and [211] directions since these two high-symmetry directions are also present in ($\bar{1}$10). The agreement of the [110] Fermi-radius determinations at 8 at. % is quite good. The [211] value is lower here than that determined from the ($\bar{1}$10) data. In this plane the Fermi surface is orthogonal to the [211] direction, unlike the situation in ($\bar{1}$10), and thus the more precise determination. This adds support to the previous statement that the ⟨113⟩ directions are developing bulges. [See Fig. 13 for the ($\bar{1}$11) slice of the Fermi surface for ^{4}Cu and $Cu_{92}Ge_8$.]

III. BAND-STRUCTURE CHANGES IN α-$Cu_{1-x}Ge_x$

A. The nature of the changes

Since the momentum density of a solid is related to all regions of the band structure and not just states near the Fermi surface, it is possible that other changes in band structure apart from Fermi-surface changes would be manifest in $\rho(\mathbf{p})$. Along the [001] direction in the gap between the first-zone Fermi break and the next HMC centered on [002], the momentum density of $Cu_{92}Ge_8$ was much larger than that of Cu and the effect extended over a wide angular region around [001], about 25°, which is somewhat larger than our 18° resolution. In an earlier paper[15] we showed that the change in this [001] region of $\rho(\mathbf{p})$ was systematic in Ge concentration. This effect is quite large when compared to the somewhat more subtle changes in the Fermi surface which occur on alloying Cu with Ge and was ascribed to an increase of *s* component in the occupied *d* bands by increased *s*-*d* hybridization when Ge is added to Cu.[15]

In order to ascertain the detectability of such changes of $\rho(\mathbf{p})$ in conduction electron gaps in other regions of momentum space or in other alloy systems, one must determine and account for the combined effect of finite experimental resolution, Fermi-surface smearing, and a changing gap size with changing electron concentration. We have done this by considering a model of the Cu(110) plane which has been chosen so as to generate data which closely match the Cu data in our experiment after convolution with our 1.8-mrad resolution. The reconstructions from the data generated by the models matched the reconstructed $\rho(\mathbf{p})$ for Cu along [100]. We then varied the Fermi radii of the model in a rigid-band way to represent Cu, $Cu_{97}Ge_3$, $Cu_{94}Ge_6$, and $Cu_{92}Ge_8$ with decreasing [100] gap widths of 2.5, 2.2, 2.0, and 1.8 mrad. The results of these "alloy" model reconstructions are shown in Fig. 14 along with the reconstructions of actual experimental data. It is immediately obvious that not only are the changes in the experimental situation much larger than those in the model, but the entire nature of the changes is different. The actual experimental results show the minimum has disappeared by the 6 at. % Ge concentration, and the $\rho(\mathbf{p})$ values for this alloy in this region have increased from the pure Cu case at least *twice* as fast as the model changes. Between 6 and 8 at. % Ge, the experimental growth rate is greater than the model's by even more than a factor of 2.

Note that the Fermi-surface smearing due to disorder scattering of the electrons has not been included above. Prasad and Bansil[21] have shown that in Cu-Ge alloys this might be considerable. They give the theoretical FWHM values of the greatest smearing to be ~0.6 mrad for the

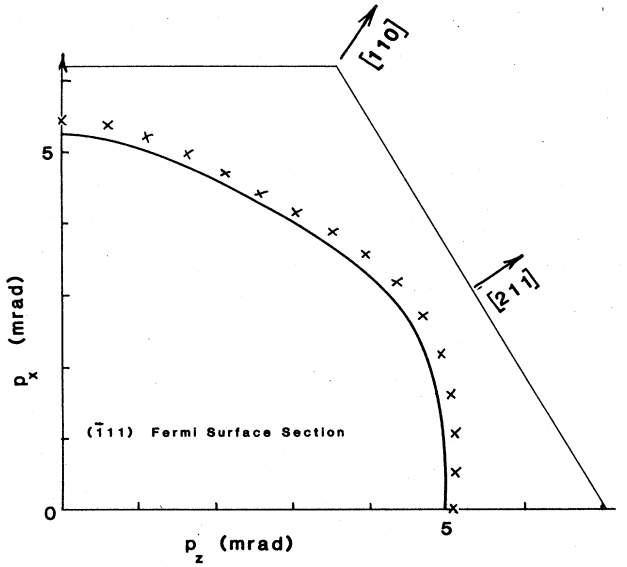

FIG. 13. ($\bar{1}$11) slice of Fermi surface for ^{4}Cu and $Cu_{92}Ge_8$ (×).

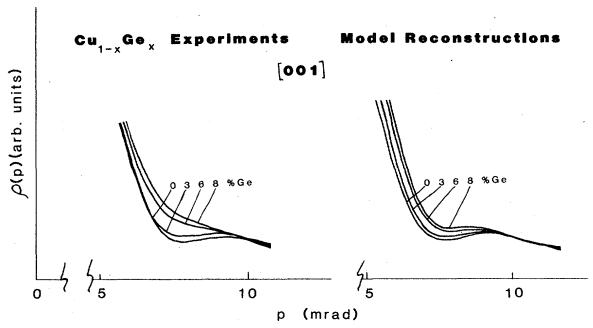

FIG. 14. Model reconstructions of $Cu_{1-x}Ge_x$ ($x=0$, 0.03, 0.06, and 0.08) compared to experimental results for the [001] gap region of $\rho(\mathbf{p})$.

case of $Cu_{92}Ge_8$. This must be convoluted with our resolution of 1.8 mrad, which is nearly Gaussian. If the smearing is nearly Gaussian, the resulting effective resolution is 1.9 mrad. This would not visibly change Fig. 14 or the conclusions that decreasing gap size coupled with resolution effects cannot explain the large changes we see along [100]. The fact that the gap in the [211] direction is not so severely affected by alloying with Ge or that none of the Fermi breaks in the other directions become less steep also argues against Fermi-surface smearing as an additional cause of the changes we find. Only extremely-high-resolution experiments will ultimately determine the true amount of Fermi-surface smearing. We therefore treat the [100] changes as resulting at least partly from band-structure changes, which we detail below.

The first to discuss the [100]/[110] anisotropies and the [100] gap was Mijnarends,[14] who produced the first direct experimental evidence for such an anisotropy between $\rho_{[110]}$ and $\rho_{[001]}$ in ^{2}Cu. He later used a Korringa-Kohn-Rostoker (KKR) calculation to produce theoretical Cu momentum densities along [001], [110], and [111].[14] Mijnarends's theoretical momentum densities also showed the [001]/[110] anisotropy and he noted that this resulted from s-d—hybridization differences between the two directions in the band structure; however, he did not go into the details of this.

With this in mind we proposed that the s-d hybridization is changing upon addition of Ge in such a way as to increase $\rho(\mathbf{p})$ in this region.[15] It should be pointed out, however, that an alternative hybridization cannot be excluded. The alloying of Cu with Ge lifts somewhat the perfect order of the pure Cu lattice. Thus, p-state character is no longer strictly prohibited at the X point of the occupied Δ band, i.e., some p state could hybridize with the occupied d band at the X point. If this p-state increase takes place at the expense of the d state (rather than the s state), then an increase in $\rho(\mathbf{p})$ entirely equivalent to that caused by an increased s-d hybridization would be seen. In order to determine the quantitative details of the changing hybridization, whichever it may be, we used an approximation to wave functions from the previously mentioned APW calculation[19,20] for the electron structure of Cu. Once we were able to determine the details of the wave function in Cu, we extended the results of the approximation to Cu-Ge alloys. Details of this not previously provided are described below.

B. APW wave functions and $\rho(\mathbf{p})$

As shown earlier[15] (with trivial changes of notation), if the plane-wave portion of the electron wave function is dropped, then the wave function in momentum space can be written

$$\chi_k^b(\mathbf{p})=\Delta(\mathbf{p}-\mathbf{k})\sum_{l=0}^{2}{}' C_l^{b,k}\phi_l(\mathbf{p}) , \tag{4}$$

where $\phi_l(\mathbf{p})=v_l(p)Y_{l0}(p)$, $\Delta(\mathbf{p}-\mathbf{k})=\sum_s \delta(\mathbf{p}-\mathbf{k}-\mathbf{K}_s)$. We then have

$$\rho(\mathbf{p})=\sum_b |\chi_k^b(\mathbf{p})|^2 . \tag{5}$$

The lth component is then $C_l^{b,k}\phi_l$, where $(C_l^{b,k})^2$ determines the fraction of ϕ_l in the wave function and ϕ_l acts like an atomic orbital. This is precisely the form of $\chi_k^b(\mathbf{p})$ one obtains in a tight-binding scheme where nearest-neighbor overlap is negligible.[23] If one deletes the p contribution from the χ's and calculates $\rho(\mathbf{p})$ in Cu using Eq. (5), the anisotropy between [001] and [110] is small and reversed compared to experimental results. Thus it is the p component which produces the observed $\rho(\mathbf{p})$ anisotropies. In fact, the p component of $\chi_k^b(\mathbf{p})$ must vanish at the Brilluoin-zone boundary in the [001] direction (the X point) in Cu by symmetry,[24] whereas at similar radial distances in the [110] direction it still contributes substantially to $\chi_k^b(\mathbf{p})$.

We can examine the situation in more detail by considering separately the $C_l^{b,k}$'s and the ϕ_l's. It turns out that, to a very good approximation, the ϕ_l's are independent of direction in $\mathbf{k}$ space and of band index (and, therefore, energy). Thus, they act much like the atomic orbitals of a tight-binding scheme. This means that the $C_l^{b,k}$'s control the shape of $\rho(\mathbf{p})$. We can calculate the fraction of s, p, or d in the wave functions in each direction by simply summing $(C_l^{b,k})^2$ over the *contributing* bands. Figure 15 shows these sums.

Figure 15 shows that the two Σ_1 bands in the [110] direction contribute 100% or 1 electron in *total* to $\rho(\mathbf{p})$ as does the one Δ_1 band in the [100] direction. The difference is that the Σ_1 bands have a slightly lower percentage of d than the Δ_1 band and a small but finite percentage of p compared to the nearly 0% p in Δ_1. The orbital ϕ_2 is much smaller than either ϕ_0 or ϕ_1 at each point $\mathbf{p}$ in the (6—7)-mrad region. The origin of the [001]/[110] anisotropy is now clear. It is this extra percentage of p in the Σ_1 bands which increases $\rho(\mathbf{p})$ for Cu in this region, making it larger than $\rho(\mathbf{p})$ along [001]. Note also from Fig. 6 that $\rho_{[110]}>\rho_{[211]}$ in the region of the [211] gap (7—9 mrad). This suggests that the hybridized Cu d bands have a maximum in their contribution to $\rho(\mathbf{p})$ along [110]. However, we have not done the calculations to show this in the directions other than [110] and [001].

The interpretation of the changes in $\rho(\mathbf{p})$ in this region upon alloying Cu with Ge have been mentioned above. We quantify them here. If we assume that the addition of

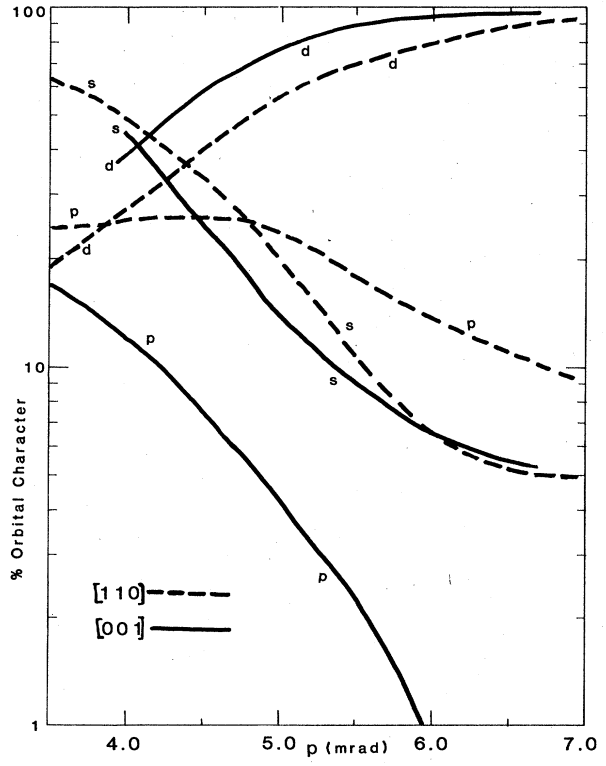

FIG. 15. Fraction s, p, and d of the wave functions of the lower d bands contributing to $\rho(\mathbf{p})$ in the "core" region.

Ge does not affect the translation symmetry in any great way, then the percentage of p is zero at X and the changes in $\rho(\mathbf{p})$ require an increase in the percentage of s in the wave functions along this direction in the [001] gap. On the other hand, if the introduction of Ge and the attendant slight lifting of the symmetry allows the appearance of a p state at X, the same changes in $\rho(\mathbf{p})$ are expected. Our experimental results and analysis of the effects of resolution broadening suggest approximately a 5% change in the percentage of s or p in the wave function at X, going from 5% to 10% s or 0% to 5% p. Finally, the appearance of a lower Δ_1 energy band in the [100] direction, suggested by CPA calculations,[21] could play an additional role in this phenomena.

IV. CONCLUSIONS

We have shown that the deconvolution-reconstruction techniques presented here are useful in elucidating features of the momentum density not easily seen in the data profiles, or which could be difficult to separate from other details because of the integration of $\rho(\mathbf{p})$ over p_x. We have taken full advantage of the two-dimensional quality of the resulting reconstruction to examine Fermiology along several radial directions and along the $K-U$ line. In general, the techniques we present here have yielded p_F values which agree well with other results (where these are available) and which suggest interesting non-rigid-band growth along several directions not usually examined in most positron-annihilation work (e.g., [113]). Our technique for normalization of the data appears to work well for these alloys. The relative size of the "core" and "conduction" volumes contributing to $\rho(\mathbf{p})$ should be representative of relative annihilation rates for the different bands, but we have not examined this closely. If such numbers could be generated from a theoretical calculation, comparison with our empirical volume ratios would be of interest.

We have showed that positron-annihilation experiments are now at the point where it is feasible and elucidating to look for changes in $\rho(\mathbf{p})$ in alloys which relate to band-structure features other than Fermi-surface details. In this case the changes are highly suggestive of hybridization changes in the bands along [001] as Ge is added to Cu. It remains to be seen whether better alloy calculations can define the nature of the changes. CPA calculations by Prasad and Bansil[21] show that, as Ge is added to Cu, a Δ_1-type band is formed which lies below the lower Cu Δ_1 band. This probably affects $\rho(\mathbf{p})$, but it is not clear how it does so at this time since only band structures and some fermiology are presented in Ref. 21.

Finally, it is interesting in light of our simple APW calculations to see how very sensitive $\rho(\mathbf{p})$ is to the admixture of s and p states into the d band. Because of the large orbital values of the s and p wave functions in momentum space, changes of a few percent in state characters are detectable. This situation should be found in most transition metals, and thus offers an opportunity to use positron annihilation to detect subtle changes in electronic structure upon alloying.

ACKNOWLEDGMENTS

We would like to acknowledge Harry S. Davis for his capable handling of the radioactive samples and his valuable assistance in sample preparation for all these experiments. We would also like to thank Taufig Raby and his National Bureau of Standards (NBS) reactor operations staff, in particular N. Bickford, for their cooperation in preparing the irradiated samples. Finally, the assistance of Dimitri Papaconstantopoulos in providing us with the APW wave functions and guiding us in the calculation of the momentum density is greatly appreciated.

[1]P. E. Mijnarends, in *Positrons in Solids,* edited by P. Hautojarvi (Springer, New York, 1979).
[2]P. E. Mijnarends, Phys. Rev. **178**, 622 (1969).
[3]S. Berko, in Proceedings of the 5th International Conference on Positron Annihilation (Japan, 1979) (unpublished).
[4]R. L. Waspe and R. N. West, in *Proceedings of the 6th International Conference on Positron Annihilation (Ft. Worth, TX),* edited by P. G. Coleman, S. C. Sharma, and L. M. Diana (North-Holland, New York, 1982).
[5]L. M. Pecora and A. C. Ehrlich, Phys. Rev. **19**, 719 (1979).
[6]E. Senicki and E. Becker, in Proceedings of the 2nd International Conference on Positron Annihilation, Kingston, Cana-

da (1971) (unpublished), p. 1.55.
[7]K. Fujiwara and O. Sueoka, J. Phys. Soc. Jpn. **21**, 1947 (1966).
[8]M. Hasegawa, T. Suzuki, and M. Hirabayashi, J. Phys. Soc. Jpn. **37**, 85 (1974).
[9]We have made Monte Carlo calculations of our resolution and the independence of the y and z variables is a very good approximation. The calculated resolution of our tube matrix collimator approached very closely the triangular resolution of the crossed-slit geometry.
[10]V. F. Turchin, V. P. Kozlov, and M. S. Malkevick, Usp. Fiz. Nauk **102**, 345 (1970) [Sov. Phys.—Usp. **13**, 681 (1971)].
[11]V. I. Goldanskii, K. Peterson, V. P. Shantarovich, and A. V. Shishkin, Appl. Phys. **16**, 413 (1978).
[12]R. A. Brooks and G. Di Chiro, Phys. Med. Biol. **21**, 689 (1976).
[13]A. Cormack, Phys. Med. Biol. **18**, 195 (1973).
[14]P. E. Mijnarends, Physica (Utrecht) **63**, 235 (1972).
[15]L. M. Pecora and A. C. Ehrlich, Phys. Rev. Lett. **46**, 1476 (1981).
[16]M. R. Halse, Proc. R. Soc. London Philos. Trans., Ser. A **265**, 507 (1969).
[17]J. G. McLarnon and D. L. Williams, J. Phys. Soc. Jpn. **43**, 1244 (1977).
[18]T. Suzuki, M. Hasegawa, and M. Hirabayashi, Appl. Phys. **5**, 269 (1974).
[19]D. A. Papaconstantopoulos, L. L. Boyer, B. M. Klein, A. R. Williams, V. L. Morruzzi, and J. F. Janak, Phys. Rev. B **15**, 4221 (1977).
[20]D. A. Papaconstantopoulos (private communication).
[21]R. Prasad and A. Bansil, Phys. Rev. Lett. **48**, 113 (1982).
[22]A. Bansil, E. Ehrenreich, L. Schwartz, and R. E. Watson, Phys. Rev. B **9**, 445 (1974).
[23]S. Berko and J. S. Plaskett, Phys. Rev. **112**, 1877 (1958).
[24]G. F. Koster, J. O. Dimmock, R. G. Wheeler, and H. Statz, *Properties of the Thirty-Two Point Groups* (MIT Press, Cambridge, MA, 1963).